BEITRAG 1 – WISSENSCHAFTSPREIS 2020

Artifact Correction and Real-Time Scatter Estimation for X-Ray Computed Tomography in Industrial Metrology

Joscha Maier[1]

*[1] Division of X-Ray Imaging and CT, German Cancer Research Center (DKFZ), Heidelberg;
RayConStruct GmbH, Nürnberg*

ABSTRACT | In recent years, computed tomography (CT) has become a valuable tool in metrology. However, the potential of CT is often limited by CT artifacts which may impair an accurate metrological assessment. To overcome this limitation, two promising approaches have been proposed recently: the so-called simulation-based artifact correction (SBAC) and the deep scatter estimation (DSE). The SBAC provides a very general framework for CT artifact correction. Given a prior model of the measured component, it performs a precise simulation of the CT measurement process including all physical effects causing artifacts. The difference between this and an ideal simulation yields an estimate of the present artifacts that can be used to correct the corresponding CT measurement. It has been shown that this approach allows to correct the most common CT artifacts, i. e. beam hardening, x-ray scattering, off-focal radiation, partial volume effects, and cone-beam artifacts. Applied to single- and multi-material measurements, it provided CT images that were almost free of artifacts and whose quality was clearly superior to common reference approaches. In this context, the problem of long runtimes of scatter simulations could be solved by the DSE using a deep convolutional neural network. Here, DSE is trained to reproduce Monte Carlo (MC) scatter estimates using only the acquired projection data as input. Once trained, DSE can be applied to unknown data in real-time and provides scatter estimates that differ from MC simulations by less than 2 %.

1   Introduction

With the rising variety and complexity of industrial components and the need for tolerance and geometrical quality control, the use of computed tomography (CT) for metrology started to be investigated in the early 1990s [1]–[3]. Providing a high measurement point density, comparably short scan times and the ability to assess internal features non-destructively, it has since become the state-of-the-art in several areas of application [4]. Despite the progress made in recent years, the investigation of highly attenuating or multi-material components remains a major challenge. As depicted in figure 1, the reconstructions of such components often show cupping, shading or streak artifacts. In general, these artifacts are caused by different physical effects that lead to a non-linear realtionship between projection values and material intersection lengths, and thus, cannot

be reconstructed exactly by analytic reconstruction algorithms. Among these effects, beam hardening, x-ray scattering, partial volume effects and off-focal radiation are the most prominent ones [5]. Another common source of artifacts is the use of circular scan trajectories in combination with a cone-beam setup. Since this trajectory only allows for an exact CT reconstruction within the mid-plane, so-called cone-beam artifacts are introduced, especially in the periphery of the reconstructed volume.

As CT artifacts often impair an accurate metrological assessment [6], artifact correction has become an active field of research. However, existing approaches are either optimized for a certain artifact, too computationally expensive to be applied routinely or they are restricted to either single- or multi-material components only. To overcome these drawbacks two promising approaches have been proposed recently by the author: the so-called simulation-based artifact correction (SBAC) and the deep scatter estimation (DSE). While the SBAC provides a very general framework to correct for most CT artifacts, DSE enables real-time scatter estimation with similar accuracy as Monte Carlo simulations. In the following both approaches are briefly reviewed, focussing on basic concepts rather than implementation details. For a more comprehensive description, the reader is referred to the original publications (reference [7], [8], and [9]).

2.   Related Work

Since the introduction of CT, there has been ongoing research on CT artifact correction. A brief overview of existing artifact correction approaches in general and scatter correction approaches in particular is given in the following section.

2.1   CT Artifact Correction

In general, artifact correction approaches can be divided into iterative approaches, post- and precorrection approaches. Iterative approaches, which have become very popular in medical CT in recent years, try to solve the reconstruction problem in an iterative manner. To do so, they usually set up a forward model that predicts projec-

Die-cast hinge   Electrical plug   Luster terminal

Model of the component

CT reconstruction

5 mm   5 mm   10 mm

C = 0.08 mm⁻¹, W = 0.18 mm⁻¹   C = 0.012 mm⁻¹, W = 0.030 mm⁻¹   C = 0.03 mm⁻¹, 0.10 mm⁻¹
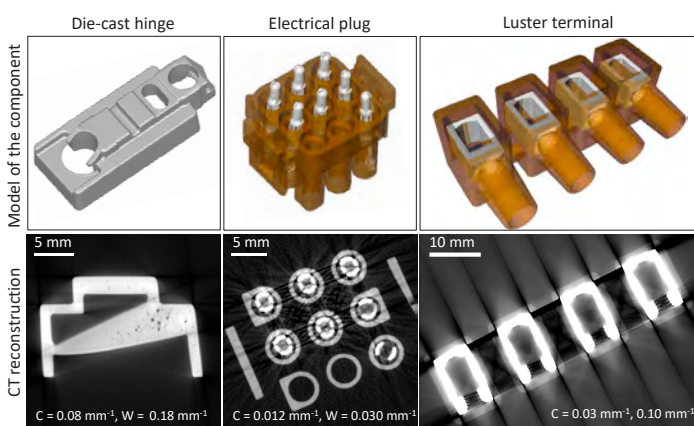
Figure 1: Models (top row) and CT reconstructions (bottom row) of typical highly attenuating (left column) and multi-material components (middle and right column). The corresponding CT reconstructions (bottom row) show severe cupping, shading and streak artifacts which impair an accurate metrological assessment.

tion data based on an estimate of the CT image. This estimate is then refined in every iteration step by calculating an update according to the discrepancy between the prediction and the measured projection data. This procedure is repeated until convergence is reached, i. e. the prediction fits the measurement. Depending on the design of the forward model, iterative approaches are able to account for the most common CT artifacts [10]–[14]. Furthermore, they allow to incorporate prior knowledge such as the shape of the measured component or image sparsity for instance [15]–[19]. However, the need for at least a few forward and backprojections makes them computationally expensive. Especially in metrological CT, which often deals with very large data sets, this is currently a major limitation.

Postcorrection approaches are often used as a faster alternative. These approaches apply physically or empircally motivated correction terms, to an analytic reconstruction. Therefore, they typically set up models with a given number of open parameters that can potentially account for a certain artifact. Subsequently, the open parameters are adjusted such that an appropriate metric, sensitive to artifacts in image domain, is minimized [20]–[23]. Therefore, no dedicated prior knowledge, such as the x-ray spectrum, is required which can be seen as a further advantage over iterative methods. More recently, the use of articial neural networks has been proposed as another realization of postcorrection approaches [24]–[26].

Besides being applied in image domain, correction terms can also be applied in projection domain prior to the reconstruction. These precorrection approaches have been proposed in several variants. Considering multi-material components that contain metal, so-called metal artifact reduction (MAR) algorithms are frequently applied. Initially MAR approaches were proposed for the correction of artifacts caused by metal implants in medical CT [27]. Their basic principle relies on the identification of the metal trace within the acquired projection data and its subsequent replacement with some sort of interpolated data [28]–[31]. The corrected projections are then reconstructed and the metal is reinserted into the CT image. While this strategy is potentially useful for multi-material components with a small amount of metal [32], interpolation errors may degrade the correction result in case of higher metal fractions.

The correction of single-material components, in contrast, often relies on approaches similar to water precorrection in clinical CT [33]. These approaches aim to map the measured projection data to ideal data which are proportional to intersection length through the object. This mapping is typically implemented by an analytic function or a look-up table that is either derived from theoretical considerations, i.e. by numerical inversion of a certain physical model describing the data acquisition, or by performing calibration measurements of a known component [34], [35]. However, strictly speaking only beam hardening artifacts can be corrected using this approach. In case of other artifacts, such as x-ray scattering or off-focal radiation, there is no unique relationship between projection values and intersection lengths. Consequently, these effects have to be considered a priori.

2.2 Scatter Estimation and Scatter Correction

There are two typical strategies to reduce the impact of scattered x-rays on CT image quality: scatter suppression and scatter estimation. The former approach is based on the use of additional hardware, such as anti-scatter grids or collimators, which are designed to reduce the number of scattered x-rays reaching the detector [36]. Scatter estimation approaches, in contrast, aim at estimating the contribution of scattered x-rays to the measured data, to subtract it subsequently [37]. One option to derive this estimate is to use dedicated hardware, e. g. primary modulation grids or beam blockers, which allow to distinguish between primary and scattered x-rays [38]–[45]. Other approaches use software-based solutions that set up empirical, physical or consistency-based models that predict or approximate x-ray scattering [21], [46]–[59].

The gold standard among these methods is Monte Carlo (MC) simulation which is able to model the entire physics of the CT data acquisition process, and thus, yields highly accurate scatter estimates [37]. On the downside, MC simulations are very time-consuming and cannot be applied in real-time using conventional hardware. Furthermore, they need prior information such as the material distribution and the density distribution that has to be estimated in advance [60].

So-called kernel-based scatter estimation (KSE) approaches are often used as a faster alternative. Basically, there are two flavors of KSE approaches. The first one estimates scattered x-rays as an integral transform of a scatter source term and a scatter propagation kernel [46], [47], [61]–[63]. The scatter source term, which is typically derived from a simplified theoretical model (e. g. only single scattering in forward direction is considered), represents the fraction of x-rays that are scattered along a straight line from the x-ray source position to a certain detector element. The scatter propagation kernel reflects the spatial spreading of scattered x-rays and is usually calibrated to fit reference measurements or MC simulations [55]. Since the multiplication of these two quantities represents the scatter distribution for a single ray, the total scatter distribution is given as the sum of all rays.

Instead of using analytic models to approximate scattering along a certain ray, other KSE approaches perform needle-beam MC simulations of primitive geometries, e. g. ellipsoids or cuboids, with varying dimensions [49], [51]–[53]. The corresponding scatter distributions are then stored as a look-up table. To estimate the x-ray scatter of a given measurement each detector pixel is assigned one of the precalculated needle-beam scatter distributions according to a similarity metric. Summing the contribution of each needle beam, including correction terms that account for the shape of the actual object, then yields the total scatter distribution [53].

While being real-time capable, KSE approaches are typically less accurate than MC simulations. Furthermore, it can be challenging to calibrate the open parameters of these models in such a way that they apply to different acquisition conditions as well as to different components. So far, there is always a trade-off between accuracy and computational performance that may be overcome by the deep scatter estimation as described in section 4.

3 Simulation-Based Artifact Correction (SBAC)

3.1 Basic Principle

Analytic CT reconstruction algorithms are based on the assumption that the projection value measured at detector position d corresponds to the following line integral:

$$p(d) = \int_0^1 d\lambda\, f(s + \lambda \cdot (d - s)), \qquad (1)$$

where s is the focal spot position and f is the CT image, i.e. the distribution of the attenuation coefficient. In that case, f can be reconstructed exactly from the set of all possible line integrals p:

$$f = X^{-1} p, \qquad (2)$$

where X^{-1} denotes the inverse x-ray transform operator which is typically implemented as filtered backprojection.

However, due to the polychromatic x-ray spectrum, off-focal radia–tion, x-ray scattering and partial volume effects, the actual data acquisition process is not modeled appropriately by equation (2).

$$
\begin{aligned}
g = X^{-1} q &= X^{-1} q + X^{-1} p - X^{-1} p \\
&= f + X^{-1}(q - p) \\
&= f + a, \qquad (3)
\end{aligned}
$$

Thus, applying the reconstruction operator X^{-1} to the measured projection data q does not yield the desired image f, but an image g containing artifacts a:

According to equation (3), a corrected image can be calculated by subtracting an estimate $\tilde{a}$ of the artifacts:

$$f_{SBAC} = g - \tilde{a} = g - X^{-1}(\tilde{q} - \tilde{p}), \qquad (4)$$

where $\tilde{p}$ and $\tilde{q}$ represent estimates of ideal and real projection data. As shown in figure 2, the SBAC derives these estimates by performing CT simulations based on a prior model f_{prior} (e.g. a CAD model or a segmentation Tg of the initial reconstruction) of the component. While ideal projection data can be calculated according to equation (1) with $f = f_{prior}$, the main challenge of the SBAC is to model the actual data acquisition process as accurately as possible. To do so, precise models have been developed or existing models have been refined. A detailed description of these models that cover the generation of x-rays, the effect and the determination of the focal spot distribution including off-focal radiation, the interaction of x-ray photons within the measured object as well as the x-ray detection process can be found in reference [7] and [9].

In a similar way, the SBAC can also account for conebeam artifacts by performing the ideal simulation as well as the corresponding reconstruction in parallel beam geometry. It has to be noted that in this case the difference between the ideal and the real simulation cannot be cal calculated in projection domain. In contrast to equation (4), the difference needs to be evaluated in image domain, i.e. the estimate of the artifacts is given by:

$$\tilde{a} = X^{-1}\tilde{q} - X_{\parallel}^{-1}\tilde{p}, \qquad (5)$$

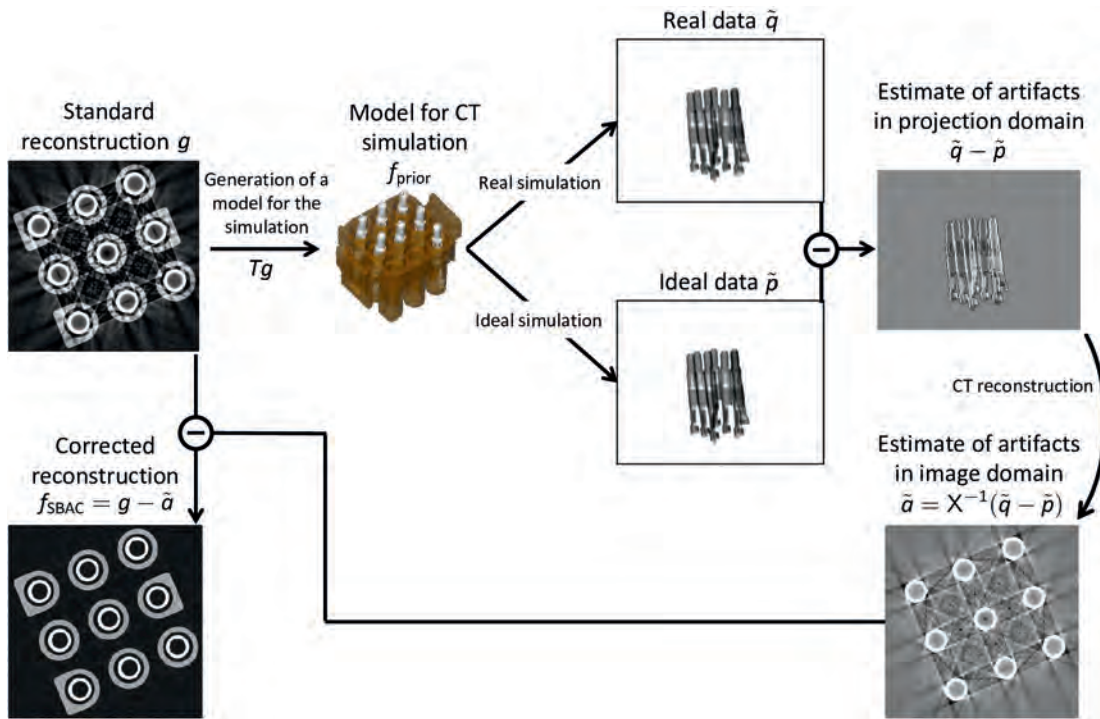where $X_{\parallel}^{-1}$ represents the reconstruction operator in parallel beam geometry.

Figure 2: Schematic of the SBAC workflow. An initial reconstruction g is used to generate a prior model. Based on that model, a real and an ideal simulation is performed. Their difference represents the artifacts within the measurement and can be used to calculate a correction term for the initial reconstruction.

Table 1: Acquisition parameters of single-material and multi-material measurements as well as the mean and the maximum intersection length (L). It has to be noted that in case of the multi-material components these measures only refer to the metal intersection length.

Sample	Voltage	Current	Prefilter	Projections per 360°	Pixel size at isocenter	Mean L / Max. L
Plug 1	225 kV	170 ųA	1.2 mm Sn	1200	41 ųm	3.0 mm / 15.9 mm
Luster terminal	225 kV	170 ųA	1.2 mm Sn	1200	41 ųm	4.9 mm / 29.8 mm
Inhalator	160 kV	90 ųA	0.5 mm Al	800	80 ųm	4.3 mm / 42.6 mm
Plug 2	225 kV	170 ųA	1.2 mm Sn	1200	25 ųm	1.1 mm / 6.8 mm
Zinc hinge	215 kV	180 ųA	1.0 mm Sn	800	43 ųm	3.8 mm / 20.5 mm

3.2 Measurements and Evaluation

To demonstrate the potential of the SBAC, it was applied to measurements of different single- and multi-material components (see figure 3). All measurements were conducted using a commercial industrial CT system (Werth TomoScope® 200) that is equipped with a 225 kV micro-focus x-ray tube and a 3888 x 3072 flat detector with a pixel size of 149.6 x 149.6 ųm in a 2 x 2 binning mode. The corresponding measurement parameters as well as the maximum and the mean intersection lengths are summarized in table 1.

Considering the single-material measurements, the focus of the evaluation was set on dimensional accuracy. Therefore, surface meshes extracted from CT reconstructions with and without SBAC were compared against (almost) artifact free reference measurements. In case of the die-cast zinc hinge, the corresponding reference measurements were performed using a commercial coordinate measurement machine (Werth Touch Probe TP 200) with a maximum permissible probing error of 2 ųm. In case of the plastic inhalator, which mainly shows cone-beam artifacts, two CT measurements were performed. One with a large cone-angle and one with a small cone-angle.

While the SBAC was applied to the large cone-angle measurement, the small cone-angle measurement which showed only minor artifacts was used as reference.

In contrast to the single-material measurements, an artifact free reference measurement could not be performed for the multi-material components. Therefore, the performance of the SBAC was evaluated qualitatively by a comparison to two state-of-the-art artifact correction approaches: the normalized matal artifact reduction (NMAR) [29] and the iTV algorithm [64]. As described in section 2, the NMAR belongs to the inpainting-based correction approaches that identify the metal trace within the acquired projection data and replace it by interpolated data. The iTV algorithm, in contrast, solves the reconstruction problem iteratively including a total variation (TV) constraint.

3.3 Results
3.3.1 Single-Material Components

CT reconstructions of the single-material components are shown in figure 4. While the uncorrected reconstruction of the zinc hinge shows strong cupping and shading artifacts, the one of the plastic inhalator is mainly corrupted by cone-beam artifacts. In any case, almost all artifacts are removed after applying the SBAC.

Since the visual impression does not necessarily correlate with the dimensional accuracy of the CT measurement, a dimensional evaluation was performed as well. For this purpose, surface meshes were extracted from the CT reconstructions and compared against the
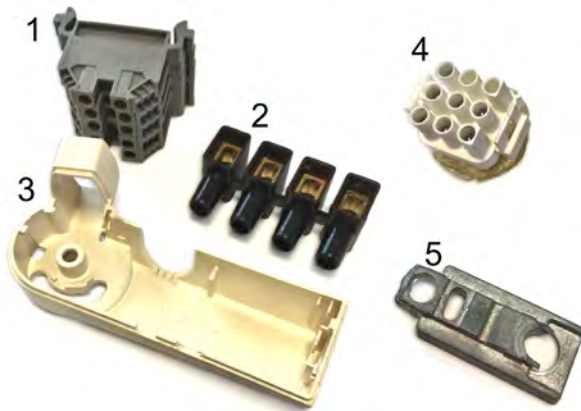

Figure 3: Photograph of the components used for testing the performance of the SBAC. 1. Electrical plug 1, 2. Luster terminal, 3. Plastic inhalator, 4. Electrical plug 2, 5. Die-cast zinc hinge.
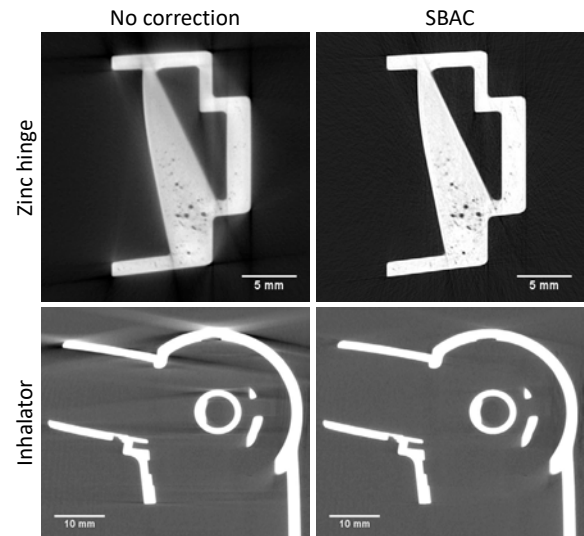

Figure 4: Reconstruction of the measured die-cast zinc hinge (top, C = 0.08 mm⁻¹ / W = 0.20 mm⁻¹) and the inhalator (bottom, C = 0.00 mm⁻¹ / W = 0.10 mm⁻¹) without and with simulation-based artifact correction (left and right).
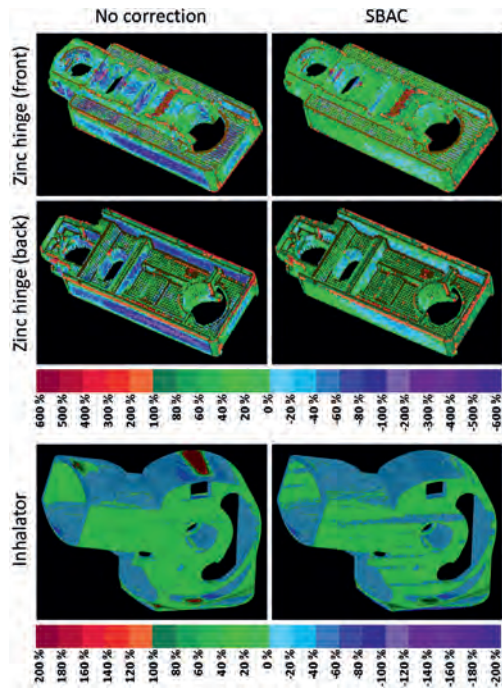
Figure 5: Dimensional evaluation of the CT measurement of the die-cast zinc hinge (top) and the inhalator (bottom) with and without simulation-based artifact correction. The color scale refers to the tolerances specified by the manufacturer. Here, 100 % and -100 % are the maximum acceptable deviations of the CT measurement from the reference measurement.

reference measurements described in section 3.2. The corresponding results are shown in figure 5. In case of the die-cast zinc hinge, there are large deviations from the tactile reference measurement that exceed the tolerances specified by the manufacturer by up to 400 %. These deviations are reduced to well below 60 % when using the

SBAC, indicating the high accuracy of the proposed approach (note that the deviations along the edges of the component result from missing sample points of the tactile measurement).

The evaluation of the inhalator measurement demonstrates the potential of the SBAC for cone-beam artifact correction. Here, the surface meshes were compared against a surface mesh calculated from a CT measurement with a narrow cone-angle. Without correction there are deviations, especially in the periphery of the field of measurement where the cone-angle is large, that exceed the tolerances of the manufacturer by more than 200 %. Applying the SBAC reduces these deviations to values well below values of 40 %.

3.3.2 Multi-Material Components

The correction of multi-material components was evaluated for three typical components with different metal fractions or metal intersection lengths, respectively (see table 1). Since multi-material components cannot be assessed entirely using a tactile probe, two commonly used artifact correction algorithms, NMAR and an iterative reconstruction with TV regularization, were implemented as a reference. The corresponding CT reconstructions as well as an analytic reconstruction and the SBAC result are shown in figure 6.

As expected, the presence of metal leads to severe streak artifacts in the analytic reconstruction. In contrast to measurements with small metal fractions, where the NMAR usually yields a considerable improvement of image quality, the correction of the present measurements is rather poor. This can be explained by the fact that the metal trace covers a large area of the projections. As a result, the interpolation approach used by the NMAR algorithm fails and even new artifacts are introduced to the CT reconstruction. Similarly, the iterative reconstruction approach does not manage to remove streak artifacts but leads to a small improvement only. In contrast, the SBAC removes almost all artifacts and yields CT volumes that allow for a clear discrimination between plastic and metal.
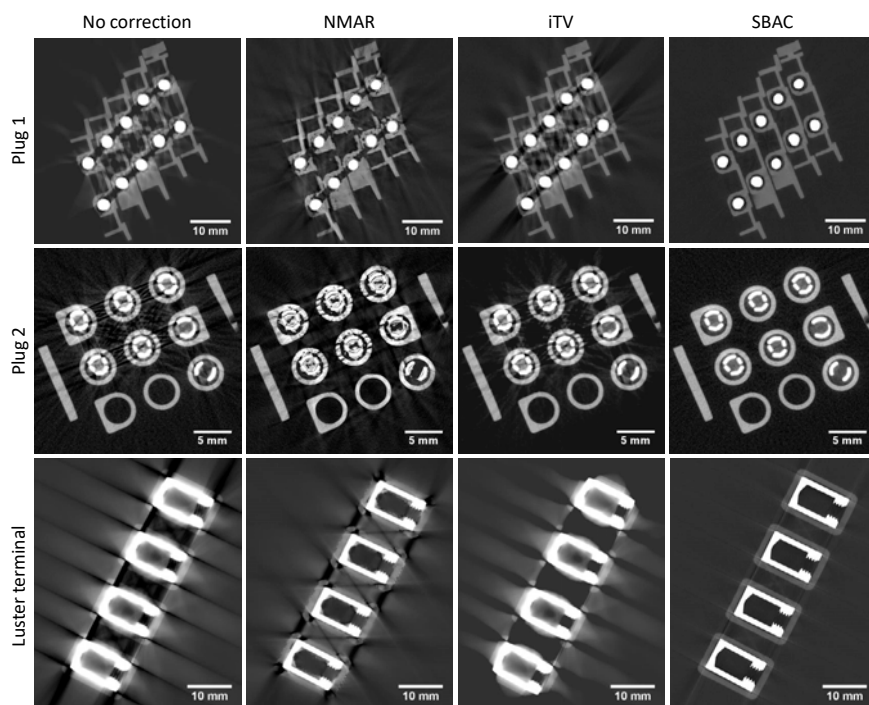

Figure 6: CT reconstructions of two different multi-material plugs (top row, $C = 0.012\ mm^{-1} / W = 0.030\ mm^{-1}$, middle row $C = 0.02\ mm^{-1} / W = 0.06\ mm^{-1}$) and a luster terminal (bottom row, $C = 0.03\ mm^{-1} / W = 0.10\ mm^{-1}$).

## 4.	Deep Scatter Estimations

### 4.1	Basic Principle

Existing Scatter estimation approaches that are real-time capable usually have the drawback of being restricted to a predefined model that is based on simplified assumptions and approximations of the x-ray scattering process. As a result, they often do not generalize well to arbitrary samples, and may not be accurate enough. More sophisticated approaches such as Monte Carlo (MC) simulations, however, are too slow to be applied routinely. To combine both, accuracy and computational performance, the so-called deep scatter estimation (DSE) has been proposed recently by the author [7], [9]. The basic idea of DSE is to train a deep convolutional neural network (DCNN) to reproduce MC scatter estimates. Therefore, DSE uses a U-net like neural network as shown in figure 7 [65], and determines it's open parameters Θ by minimizing the following loss function:

$$\boldsymbol{\theta} = \underset{\boldsymbol{\theta}}{\operatorname{argmin}} \, K \cdot \sum_n \left| \frac{\mathrm{DSE}(\psi_n, \boldsymbol{\theta}) - S_{\mathrm{MC},n}}{S_{\mathrm{MC},n}} \right|, \qquad (6)$$

where K is a normalization constant, n the sample index, ψ_n the corresponding input to the network, and $S_{\mathrm{MC},n}$ the MC scatter estimate. Since DCNNs can be implemented efficiently on a GPU, DSE can be used to perform the mapping $\psi \rightarrow S_{\mathrm{MC}}$ in real-time once the network is trained.

It has to be noted that DSE was trained and tested using different input functions ψ, namely $\psi = e^{-p}$, $\psi = p$, and $\psi = p \cdot e^{-p}$. While e^{-p} corresponds to the normalized intensities and p to their negative logarithm, $p \cdot e^{-p}$ represents an analytic estimate of forward scattering that is often used by kernel-based scatter estimation approaches [47]. Since DSE performed best using the $p \cdot e^{-p}$ input, only these results are shown here. For a more comprehensive evaluation including different inputs, the reader is referred to reference [9]

### 4.2.	Simulation Study

Considering a certain scatter estimation approach it is advantageous if it can be applied to different components and different acquisition conditions without major adjustments. The potential of DSE to do so, was investigated using CT simulations based on the models

shown in figure 8. Given the prior model, artificial projections were generated as:

$$p_{\mathrm{sim}} = -\ln\left(\frac{I + N_p + S_{\mathrm{MC}}}{I_0}\right), \qquad (7)$$

with I being the polychromatic forward projection of the prior model, N_p being Poisson distributed noise, I_0 being the flat field image, and SMC being the distribution of scattered x-rays that was calculated using our in-house Monte Carlo software. For each component a training data set and a testing data set was simulated according to the parameters given in table 2. To ensure that the training data does not resemble the testing data, it was generated using different tube voltages, different tilt angles of the component and different scaling factors.

### 4.3	Measurements

To test the application of DSE to real data, measurements of an aluminum profile were performed at our in-house table-top CT system which is equipped with a Varian 4030 flat detector and a Hamamatsu micro-focus x-ray source. There are several strategies to generate suitable training data for these measurements. Probably the most accurate way is to derive the training data from reference measurements, e.g. measurements with and without anti-scatter grid or with and without collimation. However, practically it is difficult to acquire a huge amount of data following this strategy. Therefore, simulated training data were generated using the prior models shown in figure 8. In contrast to the simulation study described in the previous section, the simulations were designed to resemble the measurement data in terms of the acquisition geometry and the acquisition conditions using the models that have been developed for the SBAC (see section 3).

### 4.4	Evaluation

The generalization of DSE to different components was evaluated using simulated data (see section 4.2). Therefore, different training data sets were generated: one containing the training data of all

Feature dimensions:

256×256	128×128	64×64	32×32	16×16	8×8	4×4	8×8	16×16	32×32	64×64	128×128	256×256

Number of features of the convolutional layer:

16	32	64	128	256	512	1024	512	256	128	64	32	16 / 1

▶ 3 × 3 Convolution (stride = 1), ReLU ▶ 3 × 3 Convolution (stride = 2), ReLU ▶ 1 × 1 Convolution (stride = 1), ReLU ◆ 2 × 2 Upsampling
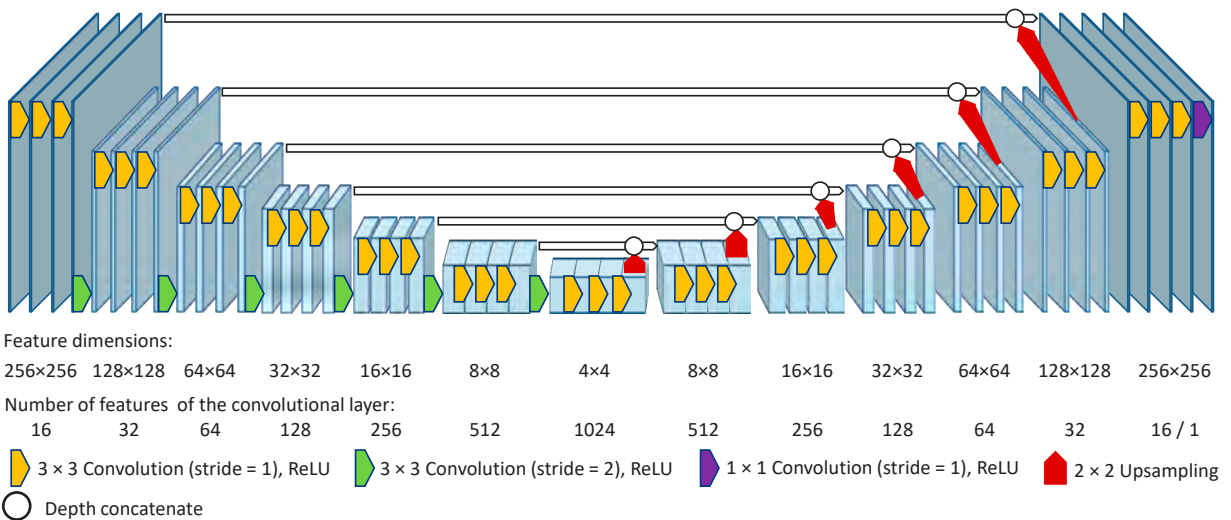
○ Depth concatenate

Figure 7: Architecture of the DSE deep convolutional neural network. Note that the network does not take the full size projection data as input, but a downsampled 256 x 256 version. Thus, the DSE scatter estimate needs to be upsampled prior to scatter correction.
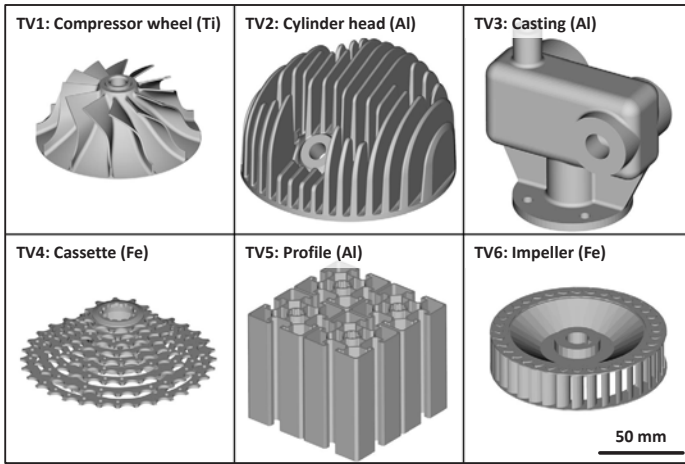
Figure 8: CAD models that were used for the generation of artificial CT data.

components, one containing the training data of the casette and the profile, and data sets containing the training data of one component only. For each training data set, the open parameters of the DSE network were determined according to equation (6). Subsequently, the performance of the networks was evaluated using the corresponding testing data sets. The accuracy of scatter predictions was quantified using the mean absolute percentage error (MAPE) with respect to the ground truth MC scatter estimate as figure of merit.

Additionally, two conventional scatter estimation approaches were implemented as reference: the kernel-based scatter estimation (KSE) [47], and the hybrid scatter estimation (HSE) [55]. These approaches derive the scatter estimate as a convolution of a scatter kernel G, with a $p \cdot e^{-p}$ image:

$$S_{KSE} = G * (p \cdot e^{-p}). \qquad (8)$$

Similar to DSE, KSE determines the open parameters of G in such a way that the scatter predictions fit the MC scatter estimates of a training data set. Once the kernel is determined, it is used for any subsequent scatter prediction. HSE, in contrast, recalibrates the kernel G for any sample to be processed. In order to achieve a reasonable computational performance, only a very coarse MC simulation is used for this recalibration.

Since there is no scatter ground truth for measured data, a slit scan acquisition with a narrow collimation was performed as a reference to evaluate the performance of the scatter correction.

5   Results
5.1   Simulation Study

Exemplary KSE, HSE and DSE scatter estimates for the the six investigated components are shown in figure 9. A quantitative evaluation of all testing data is given in table 3.

Considering a training using the data of all components, KSE shows the lowest accuracy with errors ranging from 15.4 % (casting) to 51.3 % (impeller). Since HSE calculates a distinct parameter set for every sample, the MAPE is decreased to values between 2.0 % (profile) and 8.1 % (cassette). The highest accuracy can be observed for DSE. Here, the scatter prediction is almost equal to MC simulations with a MAPE ranging from 0.8 % (casting) to 1.4 % (cassette).

Further experiments optimized the scatter estimation for one particular component only. This led to an increase of the accuracy of KSE scatter predictions, especially for highly attenuating components (compressor, cassette, impeller). In contrast, no further improvement could be observed for DSE. In any case, the accuracy decreased for components that were not contained in the training data set. However, there seems to be a material dependency. Training on one of the aluminum components only (cylinder head, casting, profile), also led to a reasonable performance for the other two components while high errors occurred for the titanium and iron components (compressor, cassette, impeller). Interestingly, the errors are smaller if training and testing are performed the other way round, i. e. training on one of the high attenuation components and testing on one of the aluminum components. This might be explained by the fact that the high attenuation components have a wider range of

Table 2: Parameters of the simulation study.

| Parameter	Training	Testing
Models (see figure 8)	TV1–TV6	TV1–TV6
Source-to-isocenter distance	250 mm, 375 mm, 500 mm	250 mm, 375 mm, 500 mm
Source-to-detector distance	1000 mm	1000 mm
View angle	0° – 360°, Δα = 10°	0°– 360°, Δα = 10°
Detector elements	1024 × 1024	1024 × 1024
Detector pixel size	0.4 mm x 0,4 mm	0.4 mm x 0,4 mm
Tube voltage	150 kV, 200 kV, 300 kV	250 kV, 350 kV
Prefilter	1 mm Sn	1 mm Sn
Detector material	1 mm CsI	1 mm CsI
Object scaling factor	0.9, 1.1	1.0
Object tilt angle	0°, 18°, 72°	36°, 54°
Object material	A1 (TV2, TV3, TV5), Ti (TV1), Fe (TV4, TV6)	A1 (TV2, TV 3, TV 5), Ti (TV1) Fe (TV4, TV 6)
Samples	11664 for every component	2592 for every component
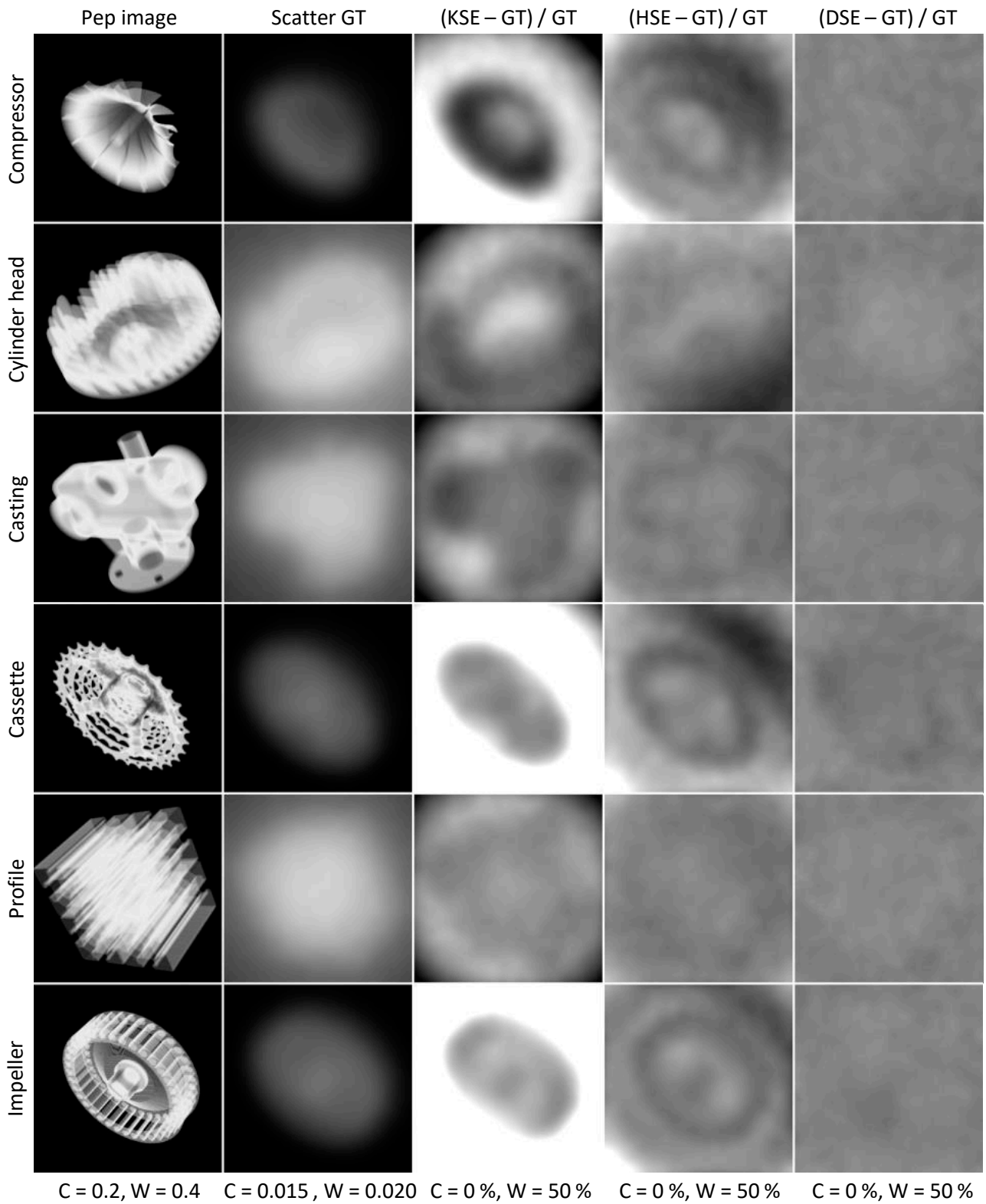
Figure 9: Percentage error of KSE, HSE and DSE scatter estimates for different components. KSE and DSE were optimized using a training data set containing all components. HSE was optimized directly for the test data.
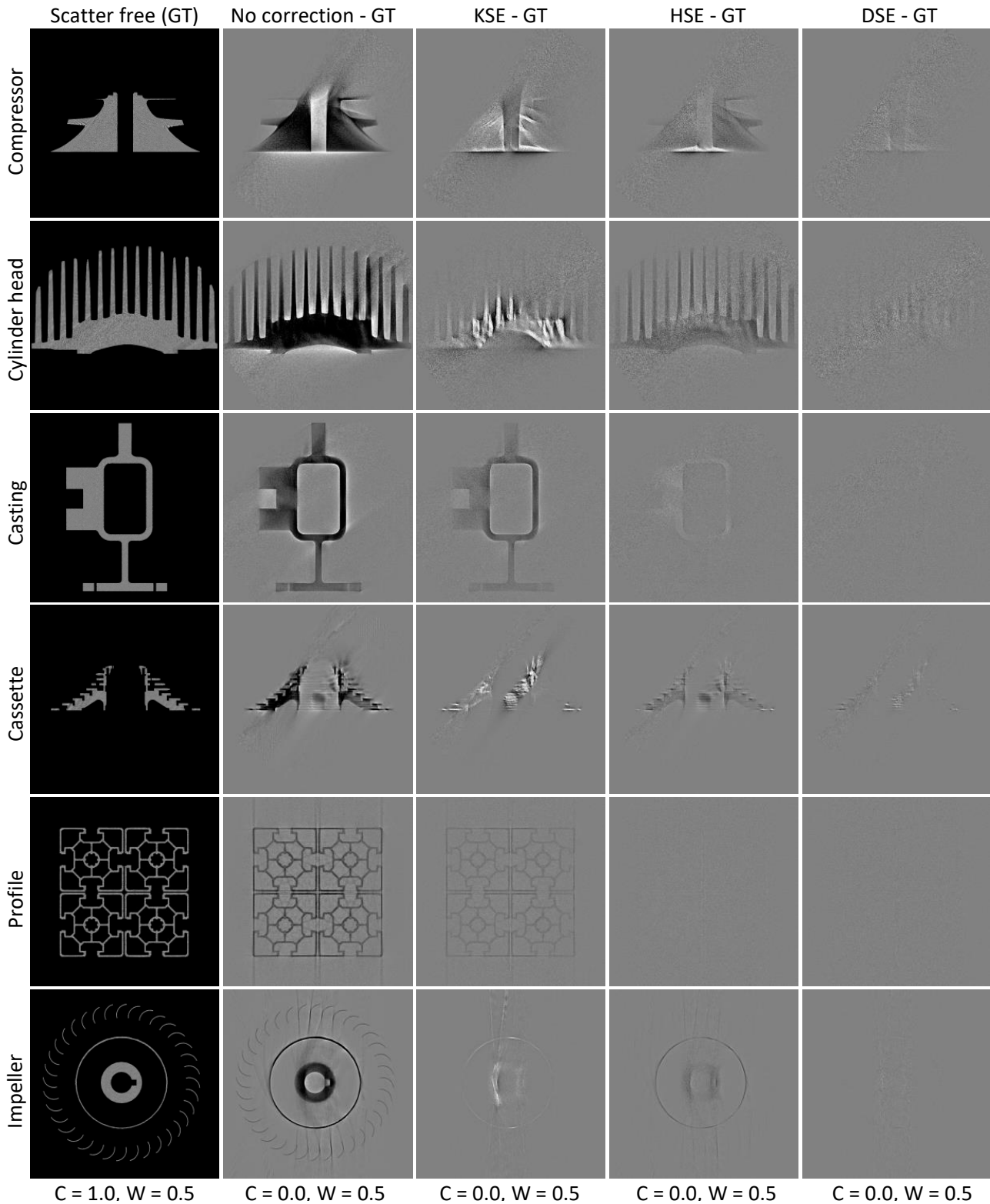
Figure 10: Scatter corrected CT reconstructions of simulated data. The simulations were performed with a tube voltage of 250 kV. Scatter was estimated using KSE, HSE and DSE and subtracted in intensity domain to get a corrected data set. Prior to reconstruction the projections were precorrected such that they represent intersection lengths. Therefore, an ideal reconstruction has a CT value equal to 1.

Table 3: Mean absolute percentage error of KSE, HSE and DSE scatter estimates for different components and different training data sets (left column). Note that there are no training data for HSE as its parameters are optimized for every sample to be processed.

	Testing Compressor	Cylinder Head	Casting	Cassette	Profile	Impeller
Training						
KSE						
Compressor	15.4	21.6	20.8	24.3	18.9	22.8
Cylinder Head	53.0	14.6	16.3	79.5	15.1	73.7
Casting	34.2	15.3	15.2	60.6	16.7	63.1
Cassette	17.5	29.9	29.1	17.3	26.9	14.9
Profile	31.5	13.9	14.1	56.7	13.7	59.3
Impeller	18.1	31.2	30.3	17.2	28.2	14.6
Profile & Cassette	26.4	15.7	15.4	47.2	13.9	49.4
All Parts	27.8	15.5	15.4	49.5	14.8	51.8
HSE						
-	7.7	5.6	3.5	8.1	2.0	5.6
DSE						
Compressor	1.3	6.1	4.0	4.3	5.3	3.8
Cylinder Head	28.1	1.0	3.8	38.1	4.9	23.4
Casting	16.3	2.3	0.9	24.9	2.1	14.3
Cassette	3.0	5.2	3.3	1.4	3.5	1.5
Profile	35.6	3.5	1.9	48.6	1.3	24.9
Impeller	5.3	8.7	5.3	4.8	6.2	1.1
Profile & Cassette	2.1	3.2	1.8	1.5	1.8	1.7
All Parts	1.2	0.9	0.8	1.4	0.9	1.1

possible projection values that potentially improves the generalization of the scatter estimation.

Furthermore, it has to be noted that training DSE only on data of two components, i.e. the profile and the cassette, yields considerably accurate scatter predictions (maximum MAPE of 3.2 %) for any other component. This suggests that DSE needs to be trained on only a few representative components to be applicable to any other measurement.

To demonstrate the impact of scatter correction on CT images, CT reconstructions were performed for the testing data. For each case scatter was estimated use KSE, HSE, and DSE and subtracted in intensity domain. To account for beamhardening, an analytic beamhardining correction was applied prior to the reconstruction. The corresponding results are shown in figure 10. Here, all three scatter estimation approaches lead to a significant improvement of the CT values. However, KSE tends to overestimate scatter in regions with a high scatter-to-primary ratio. Consequently, the attenuation of the scatter corrected projection data is overestimated as well, which leads to bright streaks in the CT reconstruction. Being recalibrated for every projection, HSE can further improve image quality but cannot completely account for all scatter artifacts. DSE, in contrast, leads to CT images that are almost equal to the scatter free ground truth.

5.2 Measured Data

To evaluate the potential of DSE as well as the reference approaches for real data, measurements were performed at our in-house table-top CT. Due to the absence of a ground truth scatter distribution, a slit scan, which was collimated to 16 detector rows, was performed as reference.

Similar to the simulation study, corrected projection data were calculated by subtracting the scatter estimate in intensity domain prior to the reconstruction. In addition to KSE, HSE, and DSE, a MC-based scatter correction was performed. The corresponding results are shown in figure 11.

Visually, all scatter estimation approaches are able to reduce the scatter-related artifacts. However, especially KSE and HSE lead to the introduction of bright streaks to the CT images. In contrast, DSE shows a similar accuracy as Monte Carlo and provides CT images that are almost equal to the slit scan.

A quantitative evaluation of the MAPE with respect to the slit scans yields similar trends. Here the following errors can be measured: 30.0 % (no correction), 15.9 % (KSE), 13.2 % (HSE), 6.0 % (DSE), and 5.8 % (MC).

However, compared to the simulation study the performance of DSE seems to be slightly lower. This may be explained by the fact that the slit scan is not completely free of scatter. Furthermore, it has to be noted that there may be additional effects causing artifacts (e. g. detector backscattering), which are currently not considered.

Slit scan | No correction | KSE
HSE | DSE | MC
C = 1.0, W = 1.0 | C = 1.0, W = 1.0 | C = 1.0, W = 1.0

Slit scan | No correction | KSE
HSE | DSE | MC
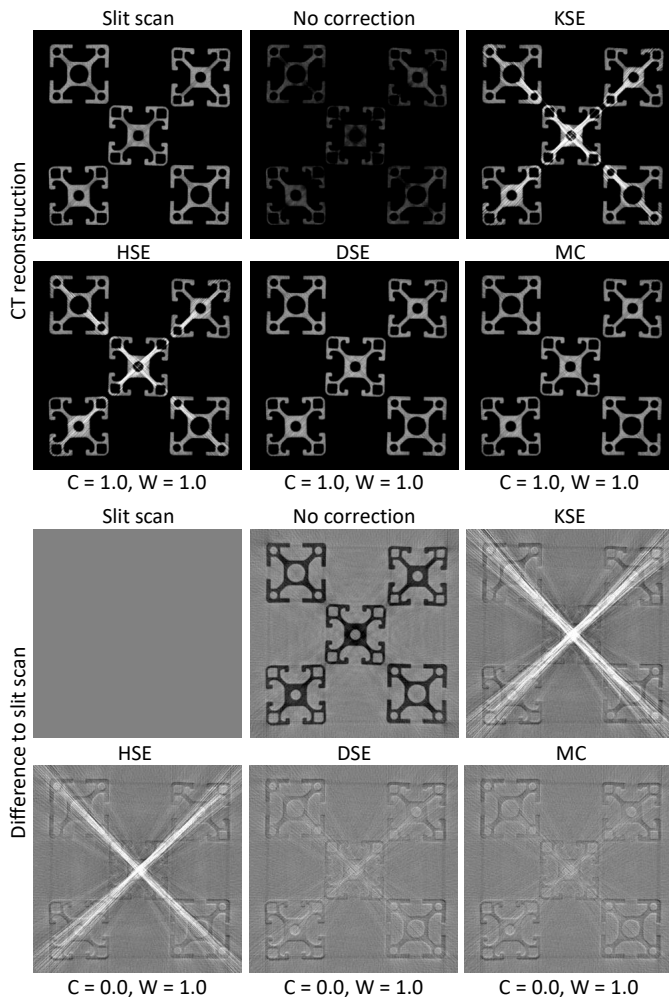C = 0.0, W = 1.0 | C = 0.0, W = 1.0 | C = 0.0, W = 1.0

Figure 11: Scatter corrected CT reconstructions of measured data. Scatter was estimated using KSE, HSE, DSE as well as a MC simulation. Prior to reconstruction the projections were precorrected such that they represent intersection lengths. Therefore, an ideal reconstruction has a CT value equal to 1.

6. Summary and Conclusion

Today, x-ray CT finds a variety of industrial applications ranging from dimensional inspection and flaw detection to reverse engineering. However, the measurement of highly attenuating or multi-material components remains a major challenge as the corresponding CT reconstructions are often corrupted by CT artifacts. Two approaches that can potentially overcome this limitation are presented in this manuscript: the simulation-based artifact correction(SBAC) and the deep scatter estimation (DSE). The SBAC provides a very general framework to correct CT artifacts using precise simulations of the CT measurement process. In this way, the SBAC accounts for any artifact that is modeled appropriately by the CT simulation. Here, the potential of the SBAC was demonstrated for the correction of beam hardening, x-ray scattering, off-focal radiation, partial volume eects and cone-beam artifacts. For measurements of single- and multi-material components, the SBAC provided CT reconstructions that showed almost no artifacts and whose quality was clearly superior to common reference approaches. Furthermore, it could be shown that the SBAC not only increases the visual impression of the CT

reconstructions, but also their dimensional accuracy. Surface meshes extracted from SBAC-corrected CT reconstructions revealed only minor deviations from tactile measurements, the gold standard in dimensional metrology. Thus, the SBAC contributes to extending the applicability of CT in the field of industrial metrology and to establishing CT as an alternative to tactile measurements even for highly attenuating components.

In the context of scatter artifact correction, the DSE was developed to solve the problem of long processing times of accurate scatter estimation approaches. Therefore, DSE trains a deep convolutional neural network to reproduce MC scatter simulations based on the measured projection data. Once, the network is trained, it can be applied to unknown data in real-time ($\approx$ 10 ms / projection). In contrast to conventional approaches, DSE does not rely on a certain theoretically motivated scattering model, but learns the most suitable model itself from observational data. This is especially an advantage if a certain scatter estimation approach needs to be adapted to novel data, e. g. data that have been acquired with different acquisition parameters or at a different system. While conventional approaches might require to refine the underlying theoretical model, DSE can be adapted by simply exchanging or extending the training data set. In order to demonstrate the practical applicability of DSE, dierent simulation studies and measurements were carried out. Here, the simulation study demonstrated that DSE generalizes well to different tube voltages, different materials, as well as different components. In particular, it could be shown that DSE is clearly superior to conventional reference methods and provides scatter distributions that deviate on average by less than 2 % from MC simulations. Furthermore, these experiments suggest that a single DSE network, trained on representative data, can be used universally for different scatter estimation tasks.

A similarly good performance could be observed for measured data of an experimental CT system. Here, DSE provided scatter-corrected CT reconstructions whose quality was almost equal to slit scan measurements. Furthermore, this study demonstrated that a DSE network, trained on simulated data, also applies to measured data.This is of particular importance as simulation is an easy way to generate an arbitrary number of training examples.

However, it has to be noted that several efforts have been made here to tune the simulations to reproduce measurements of the experimental CT system. To which extent the simulation must match the measured data is the subject of further investigations.

Obviously, if a sufficiently accurate simulation is practically not possible, DSE can also be trained using measured data, e. g. of a slit scan or a beam blocker measurement. Conceptually, there are no restrictions for the generation of training data.

Thus, DSE makes an important contribution to improve the accuracy of x-ray scatter correction, especially in case of time-critical applications such as inline-CT measurements, which require real-time capable correction approaches.

REFERENCES

[1] G. Georgeson and R. Bossi, "X-ray CT for quantitative casting material evaluation", NDT & E International, volume 27, number 2, page 101, 1994.

[2] S. T. Neel, D. S. Eliasen, and R. N. Yancey, "Dimensional measurement of internal features in complex castings", in Review of Progress in Quantitative Nondestructive Evaluation, Boston, MA: Springer US, 1995, pages 689-694.

[3] S. Trent Neel, R. Gibson, C. R. Daniels, and E. L. Klosterman, "Dimensional accuracy in X-ray computed tomography imaging", in Review of Progress in Quantitative Nondestructive Evaluation, Boston, MA: Springer US, 1998, pages 411-412.

[4] L. De Chire, S. Carmignato, J.-P. Kruth, R. Schmitt, and A. Weckenmann, "Industrial applications of computed tomography", CIRP Annals-Manufacturing Technology, volume 63, number 2, pages 655-677, 2014.

[5] J. F. Barrett and N. Keat, "Artifacts in CT: Recognition and avoidance", Radiographics, volume 24, number 6, pages 1679-91, 2004.

[6] J. J. Lifton, A. A. Malcolm, and J. W. McBride, "An experimental study on the influence of scatter and beam hardening in x-ray CT for dimensional metrology", Measurement Science and Technology, volume 27, number 1, pages 192-199, 2016.

[7] J. Maier, C. Leinweber, S. Sawall, H. Stoschus, F. Ballach, T. Müller, M. Hammer, R. Christoph, and M. Kachelrie Computertomographie, "Simulation-based artifact correction (SBAC) for metrological computed tomography", Measurement Science and Technology, volume 28, number 6, page 065 011, 2017.

[8] J. Maier, S. Sawall, M. Knaup, and M. Kachelrie Computertomographie, "Deep scatter estimation (DSE): Accurate real-time scatter estimation for X-ray CT using a deep convolutional neural network", Journal of Nondestructive Evaluation, volume 37, number 3, page 57, 2018.

[9] J. Maier, "Artifact Correction and Real-Time Scatter Estimation for X-Ray Computed Tomography in Industrial Metrology", PhD thesis, Heidelberg University, 2019.

[10] J. Nuyts, B. De Man, J. A. Fessler, W. Zbijewski, and F. J. Beekman, "Modelling the physics in the iterative reconstruction for transmission computed tomography.", Physics in Medicine and Biology, volume 58, number 12, R63-96, 2013.

[11] L. Brabant, E. Pauwels, M. Dierick, D. Van Loo, M. Boone, and L. Van Hoorebeke, "A novel beam hardening correction method requiring no prior knowledge, incorporated in an iterative reconstruction algorithm", NDT & E International, volume 51, pages 68-73, 2012.

[12] L. Brabant, M. Dierick, E. Pauwels, M. N. Boone, and L. Van Hoorebeke, "EDART, a discrete algebraic reconstructing technique for experimental data obtained with high resolution computed tomography.", Journal of X-ray Science and Technology, volume 22, number 1, pages 47-61, 2014.

[13] Y. Zhao and M. Li, "Iterative beam hardening correction for multi-material objects", PLOS ONE, volume 10, number 12, L. Zeng, Ed., e0144607, 2015.

[14] K. Dremel and T. Fuchs, "Scatter simulation and correction in computed tomography: A reconstruction-integrated approach modelling the forward projection", NDT & E International, volume 86, pages 132-139, 2017.

[15] E. Y. Sidky and X. Pan, "Image reconstruction in circular cone-beam computed tomography by constrained, total-variation minimization.", Physics in Medicine and Biology

[16] J. W. Stayman, Y. Otake, J. L. Prince, A. J. Khanna, and J. H. Siewerdsen, "Model-based tomographic reconstruction of objects containing known components", IEEE Transactions on Medical Imaging, volume 31, number 10, pages 1837-1848, 2012.

[17] J. W. Stayman, H. Dang, Y. Ding, and J. H. Siewerdsen, "PIRPLE: a penalized-likelihood framework for incorporation of prior images in CT reconstruction", Physics in Medicine and Biology, volume 58, number 21, page 7563, 2013.

[18] M. Schrapp, T. Scharrer, M. Goldammer, S. J. Rupitsch, A. Sutor, H. Ermert, and R. Lerch, "Artifact reduction in non-destructive testing by means of complementary data fusion of X-ray computed tomography and ultrasonic pulse-echo testing", Measurement Science and Technology, volume 24, number 12, page 125 403, 2013.

[19] Y. Liu, A. Beyer, P. Schuetz, J. Hofmann, A. Flisch, and U. Sennhauser, "Cooperative data fusion of transmission and surface scan for improving limited- angle computed tomography reconstruction", NDT & E International, volume 83, pages 24-31, 2016.

[20] M. Kachelrieß, K. Sourbelle, and W. A. Kalender, "Empirical cupping correction: A first-order raw data precorrection for cone-beam computed tomography", Medical Physics, volume 33, number 5, pages 1269-1274, 2006.

[21] E. Meyer, C. Maaß, M. Baer, R. Raupach, B. Schmidt, and M. Kachelrieß, "Empirical scatter correction (ESC): A new CT scatter correction method and its application to metal artifact reduction", in IEEE Medical Imaging Conference, 2010, pages 2036-2041.

[22] H. S. Park, D. Hwang, and J. K. Seo, "Metal artifact reduction for polychromatic x-ray CT based on a beam-hardening corrector", IEEE Transactions on Medical Imaging, volume 35, number 2, pages 480-487, 2016.

[23] Y. Kyriakou, E. Meyer, D. Prell, and M. Kachelrieß, "Empirical beam hardening correction (EBHC) for CT", Medical Physics, volume 37, number 10, pages 5179-5187, 2010.

[24] S. Xu and H. Dang, "Deep residual learning enabled metal artifact reduction in CT", in Proceedings of the SPIE Medical Imaging Conference, 2018.

[25] H. Yu, Y. Zhang, and Y. Chu, "Reduction of metal artifacts in x-ray CT images using a convolutional neural network", in SPIE Optical Engineering and Applications, 2017.

[26] Y. Zhang and H. Yu, "Convolutional neural network based metal artifact reduction in X-ray computed tomography", IEEE Transactions on Medical Imaging, volume 37, number 6, pages 1370-1381, 2018.

[27] W. A. Kalender, R. Hebel, and J. Ebersberger, "Reduction of CT artifacts caused by metallic implants", Radiology, volume 164, number 2, pages 576-577, 1987.

[28] A. H. Mahnken, R. Raupach, J. E. Wildberger, B. Jung, N. Heussen, T. G. Flohr, R. W. Günther, and S. Schaller, "A new algorithm for metal artifact reduction in computed tomography", Investigative Radiology, volume 38, number 12, pages 769-775, 2003.

[29] E. Meyer, R. Raupach, M. Lell, B. Schmidt, and M. Kachelrieß, "Normalized metal artifact reduction (NMAR) in computed tomography", Medical Physics, volume 37, number 2010, pages 5482-5493, 2012.

[30] E. Meyer, R. Raupach, M. Lell, B. Schmidt, and M. Kachelrieß, "Frequency split metal artifact reduction (FSMAR) in computed tomography", Medical Physics, volume 39, number 4, page 1904, 2012.

[31] J. Wang, S. Wang, Y. Chen, J. Wu, J.-L. Coatrieux, and L. Luo, "Metal artifact reduction in CT using fusion based prior image.", Medical Physics, volume 40, number 8, page 081 903, 2013.

[32] A. Amirkhanov, C. Heinzl, M. Reiter, J. Kastner, and E. Groller, "Projection-based metal-artifact reduction for industrial 3D X-ray computed tomography", IEEE Transactions on Visualization and Computer Graphics, volume 17, number 12, pages 2193-2202, 2011.

[33] G. T. Herman, "Correction for beam hardening in computed tomography", Physics in Medicine and Biology, volume 24, number 1, pages 81-106, 1979.

[34] P. Hammersberg and M. Mångård, "Correction for beam hardening artefacts in computerised tomography.", Journal of X-Ray Science and Technology, volume 8, number 1, pages 75-93, 1998.

[35] M. Krumm, S. Kasperl, and M. Franz, "Reducing non-linear artifacts of multi-material objects in industrial 3D computed tomography", NDT & E International, volume 41, number 4, pages 242-251, 2008.

[36] E.-P. Rührnschopf and K. Klingenbeck, "A general framework and review of scatter correction methods in x-ray cone-beam computerized tomography. Part 1: Scatter compensation approaches", Medical Physics, volume 38, number 7, pages 4296-4311, 2011.

[37] E.-P. Rührnschopf and K. Klingenbeck, "A general framework and review of scatter correction methods in cone-beam CT. Part 2: Scatter estimation approaches", Medical Physics, volume 38, number 9, pages 5186-5199, 2011.

[38] R. Ning, X. Tang, and D. Conover, "X-ray scatter correction algorithm for cone-beam CT imaging", Medical Physics, volume 31, number 5, pages 1195-1202, 2004.

[39] L. Zhu, N. Strobel, and R. Fahrig, "X-ray scatter correction for cone-beam CT using moving blocker array", in Proceedings of the SPIE Medical Imaging Conference, M. J. Flynn, Ed., volume 5745, 2005, page 251.

[40] L. Zhu, N. R. Bennett, and R. Fahrig, "Scatter correction method for X-ray ct using primary modulation: Theory and preliminary results", IEEE Transactions on Medical Imaging, volume 25, number 12, pages 1573-1587, 2006.

[41] K. Schorner, M. Goldammer, K. Stierstorfer, J. Stephan, and P. Boni, "Scatter correction method by temporal primary modulation in X-ray CT", IEEE Transactions on Nuclear Science, volume 59, number 6, pages 3278-3285, 2012.

[42] R. Grimmer, R. Fahrig, W. Hinshaw, H. Gao, and M. Kachelrieß, "Empirical cupping correction for ct scanners with primary modulation (ECCP)", Medical Physics, volume 39, number 2, pages 825-831, 2012.

[43] L. Ritschl, R. Fahrig, M. Knaup, J. Maier, and M. Kachelrieß, "Robust primary modulation-based scatter estimation for cone-beam CT", Medical Physics, volume 42, number 1, pages 469-478, 2015.

[44] S. Hsieh, "Estimating scatter in cone-beam CT with striped ratio grids: A preliminary investigation", Medical Physics, volume 43, number 9, pages 5084-5092, 2016.

[45] B. Bier, M. Berger, A. Maier, M. Kachelrieß, L. Ritschl, K. Müller, J.-h. Choi, and R. Fahrig, "Scatter correction using a primary modulator on a clinical angiography C-arm CT system", Medical Physics, volume 44, number 9, e125-e137, 2017.

[46] W. Swindell and P. M. Evans, "Scattered radiation in portal images: A Monte Carlo simulation and a simple physical model", Medical Physics, volume 23, number 1, pages 63-73, 1996.

[47] B. Ohnesorge, T. Flohr, and K. Klingenbeck-Regn, "Efficient object scatter correction algorithm for third and fourth generation CT scanners", European Radiology, volume 9, number 3, pages 563-569, 1999.

[48] W. Zbijewski and F. Beekman, "Fast scatter estimation for cone-beam X-ray CT by combined Monte Carlo tracking and Richardson-Lucy fitting", IEEE Medical Imaging Conference, volume 5, number C, pages 2774-2777, 2004.

[49] H. Li, R. Mohan, and X. R. Zhu, "Scatter kernel estimation with an edge-spread function method for cone-beam computed tomography imaging", Physics in Medicine and Biology, volume 53, number 23, pages 6729-6748, 2008.

[50] G. Poludniowski, P. M. Evans, V. N. Hansen, and S. Webb, "An efficient Monte Carlo-based algorithm for scatter correction in keV cone-beam CT", Physics in Medicine and Biology, volume 54, number 12, pages 3847-3864, 2009.

[51] J. Star-Lack, M. Sun, A. Kaestner, R. Hassanein, G. Virshup, T. Berkus, and M. Oelhafen, "Efficient scatter correction using asymmetric kernels", in Proceedings of the SPIE Medical Imaging Conference, E. Samei and J. Hsieh, Eds., volume 7258, 2009, 72581Z.

[52] M. Meyer, W. A. Kalender, and Y. Kyriakou, "A fast and pragmatic approach for scatter correction in flat-detector CT using elliptic modeling and iterative optimization", Physics in Medicine and Biology, volume 55, number 1, pages 99-120, 2010.

[53] M. Sun and J. M. Star-Lack, "Improved scatter correction using adaptive scatter kernel superposition", Physics in Medicine and Biology, volume 55, number 22, pages 6695-6720, 2010.

[54] W. Yao and K. W. Leszczynski, "An analytical approach to estimating the first order scatter in heterogeneous medium. II. A practical application", Medical Physics, volume 36, number 7, pages 3157-3167, 2009.

[55] M. Baer and M. Kachelrieß, "Hybrid scatter correction for CT imaging", Physics in Medicine and Biology, volume 57, number 21, pages 6849-6867, 2012.

[56] A. Sossin, V. Rebuffel, J. Tabary, J. M. L´etang, N. Freud, and L. Verger, "A novel scatter separation method for multi-energy x-ray imaging", Physics in Medicine and Biology, volume 61, number 12, pages 4711-4728, 2016.

[57] A. Maslowski, A. Wang, M. Sun, T. Wareing, I. Davis, and J. Star-Lack, "Acuros CTS: A fast, linear Boltzmann transport equation solver for computed tomography scatter - part I: Core algorithms and validation", Medical Physics, volume 45, number 5, pages 1899-1913, 2018.

[58] A. Wang, A. Maslowski, P. Messmer, M. Lehmann, A. Strzelecki, E. Yu, P. Paysan, M. Brehm, P. Munro, J. Star-Lack, and D. Seghers, "Acuros CTS: A fast, linear Boltzmann transport equation solver for computed tomography scatter – part II: System modeling, scatter correction, and optimization.", Medical Physics, volume 45, number 5, pages 1914-1925, 2018.

[59] M. Hoffmann, W. Tobias, N. Maaß, F. Dennerlein, and A. Maier, "Empirical scatter correction using the epipolar consistency condition", in 5th International Conference on Image Formation in X-Ray Computed Tomography, 2018.

[60] N. Waltrich, S. Sawall, J. Maier, J. Kuntz, K. Stannigel, K. Lindenberg, and M. Kachelrieß, "Effect of detruncation on the accuracy of Monte Carlo-based scatter estimation in truncated CBCT", Medical Physics, volume 45, number 8, pages 3574-3590, 2018.

[61] L. A. Love and R. A. Kruger, "Scatter estimation for a digital radiographic system using convolution filtering", Medical Physics, volume 14, number 2, pages 178-185, 1987.

[62] L. Spies, M. Ebert, B. a. Groh, B. M. Hesse, and T. Bortfeld, "Correction of scatter in megavoltage cone-beam CT", Physics in Medicine and Biology, volume 46, number 3, pages 821-833, 2001.

[63] J. Rinkel, L. Gerfault, F. Est`eve, and J.-M. Dinten, "A new method for x-ray scatter correction: first assessment on a cone-beam CT experimental setup", Physics in Medicine and Biology, volume 52, number 15, pages 4633-4652, 2007.

[64] L. Ritschl, F. Bergner, C. Fleischmann, and M. Kachelrieß, "Improved total variation-based CT image reconstruction applied to clinical data.", Physics in Medicine and Biology, volume 56, number 6, pages 1545-1561, 2011.

[65] O. Ronneberger, P. Fischer, and T. Brox, "U-Net: convolutional networks for biomedical image segmentation", Medical Image Computing and Computer-Assisted Intervention, pages 234-241, 2015.